RESEARCH ARTICLE | AUGUST 18 2023

## Analytical theory for a droplet squeezing through a circular pore in creeping flows under constant pressures

Zhengxin Tang (唐正昕) ⑩ ; François Yaya ⑩ ; Ethan Sun ⑩ ; Lubna Shah; Jie Xu (徐杰) ⑩ ; Annie Viallat ⑩ ; Emmanuèle Helfer ⑩ ; Zhangli Peng (彭张立) ☎ ⑩



Physics of Fluids 35, 082016 (2023) https://doi.org/10.1063/5.0156349





CrossMark

#### Articles You May Be Interested In

End loss for Stokes flow through a slippery circular pore in a barrier of finite thickness

Physics of Fluids (October 2018)

Fusion and consonance relations for tones with inharmonic partials

J Acoust Soc Am (August 2005)

A New And Improved Version Of HULLAC

AIP Conference Proceedings (August 2007)



# Analytical theory for a droplet squeezing through a circular pore in creeping flows under constant pressures

Cite as: Phys. Fluids **35**, 082016 (2023); doi: 10.1063/5.0156349 Submitted: 28 April 2023 · Accepted: 28 July 2023 · Published Online: 18 August 2023







Zhengxin Tang (唐正昕),¹ [iɒ François Yaya,² [iɒ Ethan Sun,³ [iɒ Lubna Shah,¹ Jie Xu (徐杰),¹ [iɒ Annie Viallat,² [iɒ Emmanuèle Helfer,² [iɒ and Zhangli Peng (彭张立)¹.a¹ [iɒ

#### **AFFILIATIONS**

- <sup>1</sup>Richard and Loan Hill Department of Biomedical Engineering, University of Illinois at Chicago, 1200 W Harrison St, Chicago, Illinois 60607, USA
- <sup>2</sup>Aix Marseille Univ, CNRS, (Centre Interdisciplinaire de Nanoscience de Marseille) CINAM, Turing Centre for Living Systems, Marseille, France

#### **ABSTRACT**

We derived equations and closed-form solutions of transit time for a viscous droplet squeezing through a small circular pore with a finite length at microscale under constant pressures. Our analyses were motivated by the vital processes of biological cells squeezing through small pores in blood vessels and sinusoids and droplets squeezing through pores in microfluidics. First, we derived ordinary differential equations (ODEs) of a droplet squeezing through a circular pore by combining Sampson flow, Poiseuille flow, and Young–Laplace equations and took into account the lubrication layer between the droplet and the pore wall. Second, for droplets wetting the wall with small surface tension, we derived the closed-form solutions of transit time. For droplets with finite surface tension, we solved the original ODEs numerically to predict the transit time. After validations against experiments and finite element simulations, we studied the effects of pressure, viscosity, pore/droplet dimensions, and surface tension on the transit time. We found that the transit time is inversely linearly proportional to pressure when the surface tension is low compared to the critical surface tension for preventing the droplet to pass and becomes nonlinear when it approaches the critical tension. Remarkably, we showed that when a fixed percentage of surface tension to critical tension is applied, the transit time is always inversely linearly proportional to pressure, and the dependence of transit time on surface tension is nonmonotonic. Our results provided a quick way of quantitative calculations of transit time for designing droplet microfluidics and understanding cells passing through constrictions.

Published under an exclusive license by AIP Publishing. https://doi.org/10.1063/5.0156349

#### I. INTRODUCTION

Droplets passing through constricted channels have been widely studied in various applications such as microfluidics and biomedical engineering. <sup>1–8</sup> Furthermore, biological cells passing through small constrictions under *in vivo* conditions have been investigated, including the splenic clearance of red blood cells, <sup>9,10</sup> white blood cell diapedesis, <sup>11</sup> and cancer cell metastasis. <sup>12–14</sup> Understanding the transit dynamics of deformable objects such as bubbles, droplet, or cells, through constrictions is crucial, e.g., for industry to prepare controlled suspensions or for engineering of biomimetic objects for biological applications. Specifically, for cells, *in vivo* studies on their passage through constrictions, such as red blood cells passing through splenic

sub micrometer-wide slits<sup>15,16</sup> or red blood cell precursors egressing through bone marrow sub micrometer slits,<sup>17</sup> are too invasive, thus limiting the panel of available measurements. Microfluidic approaches that have emerged in the past 20 years have broadened the possibilities, allowing them to mimic physiological situations and to observe transiting cells in real time.<sup>10,18,19</sup> Still, it is not possible to vary all parameters in the *in vitro* systems and to explore all situations. The major drawbacks are the laborious fabrication of the microfluidic devices with specific features, such as sub micrometer-wide slits<sup>19</sup> and the sometimes difficult image analysis of cell deformation and dynamics, which cannot be always automated due to low image contrast or unstable cell focus.<sup>20</sup> Thus, the ongoing development of analytical and numerical models allows further exploration of conditions that are not

<sup>&</sup>lt;sup>3</sup>Phillips Academy, 180 Main St, Andover, Massachusetts 01810, USA

a) Author to whom correspondence should be addressed: zhpeng@uic.edu

experimentally reachable. In all these *in vivo* and *in vitro* cases, the speed at which droplets or cells pass through the constrictions is crucial. For example, the slowing down of red blood cells passing through the inter-endothelial slits can cause premature capture and removal by macrophages, which can lead to anemia. Pala Accurate controlling of the speed of droplets in microfluidic devices is also important for manipulation and separations, and in these cases, there is always a lubrication layer. We focus on the current situations of droplets under flow in confined environments, typical of digital microfluidics applications, and blood cells in the network of blood capillaries. In these cases, a lubrication layer exists between drops/capsules/cells and the wall to preserve the integrity of the objects in the channels/vessels and prevent physicochemical interactions and adhesion to the wall.

So far, however, the transit velocity and its dependences on various parameters quantitatively remains unclear. In this study, we will focus on this unsolved issue for the specific case of a droplet with constant surface tension in a low Reynolds number flow with a lubrication layer.

Experimental studies have been carried out to understand how droplets, vesicles, and cells pass through constrictions. For example, Ma et al. studied the flow topology inside droplets moving in rectangular microchannels.<sup>22</sup> Wang et al. discussed how a viscous droplet behaves in a Y shaped capillary channel.<sup>23</sup> Gregersen et al. investigated how red blood cells pass through small pores created on a paper.<sup>24</sup> Gambhire et al. explored red blood cells passing through sub micrometer-wide slits that mimic the splenic slits. 19 Ren et al. created a microfluidic device to study biophysical attributes and transit times of cells passing through constriction regions.<sup>25</sup> To relate passage time and viscosity, Khan et al. studied the confined flow of cancer cells and viscous droplets in microchannels.<sup>26</sup> However, it is often difficult to experimentally measure or image the deformation and dynamics of droplet/cells in small constrictions, and no clear relation between constriction size, viscosity, applied pressure, and surface tension has emerged.

In addition to experimental studies, theoretical and computational investigations have been carried out to understand the transit processes of various deformable objects. Zhang et al. developed analytical models to study the pressure and the minimum impulse of a droplet passing through a circular pore under constant flow rate. 27-29 In addition, Jensen et al. applied an energy approach to study a bubble squeezed through a short constriction<sup>30</sup> and Marmur analyzed a droplet penetrating through a capillary under gravity.<sup>31</sup> Gompper and Kroll developed an analytical solution to model the mobility of vesicles squeezing through a cylindrical pore past a threshold driving field strength.<sup>32</sup> Finally, Waugh and Sassi developed an analytical model of red blood cell egress in bone marrow to estimate their transit time.<sup>33</sup> In addition to passing through a constricted pore, there were classical papers of applying lubrication theories to study bubbles, droplets, vesicles, and red blood cells moving in cylindrical tubes, 34-36 which provided ways to consider the lubrication layer between droplets and walls. However, the existing analytical studies often use constant flow rates, which is not the pressure drop parameter used in the experimental study. For example, in the studies by Zhang et al., 27flow rate is assumed but in many practical applications, constant pressure drop is usually prescribed. In addition, most applications occur at the micrometer scale so that the generated flows should be creeping flows rather than finite Reynolds number flows, which were considered in Zhang et al.27

In addition to analytical models, various numerical methods were employed to study the passage of droplets, vesicles, and cells through microfluidic pores,<sup>37</sup> which was reviewed in Zhang *et al.*<sup>38</sup> For example, Barthes-Biesel conducted pioneer work on applying boundary integral simulations to study vesicles and capsules passing through constrictions under axisymmetric configuration. Zinchenko and Davis<sup>39</sup> applied a similar approach to study the 3D case of a droplet passing through the constrictions between spheres. However, these simulations involving solving partial differential equations (PDEs) are extremely expensive, especially in 3D. In many cases, it is impossible to resolve the thin lubrication layer with limited computational resources.

In summary, despite the existing experimental, theoretical, and computational studies above, it is still not clear how exactly the transit time changes with the pore dimensions, pressure, viscosity, and surface tension in the very current situations of low Reynolds number with the presence of a lubrication layer.

To address these unresolved issues, here we developed analytical models of droplets passing through constrictions with circular cross sections under constant pressure drops and with a lubrication layer between the droplet and the constriction walls. In specific conditions of wetting droplets with small surface tension, the analytical model is simplified to derive exact solutions of transit time. Apart from these conditions, the problem is solved numerically to study the impact of flow conditions and droplet properties on transit time. Only constant surface tension is considered here and not vesicles' or cells' specific features, such as membrane viscosity and stiffness, which may play a crucial role. The pore geometry is circular and not rectangular such as in the case of red blood cells filtered by the spleen and exiting through inter-endothelial slits. Nevertheless, our model gives a first approximate solution that paves the way to further implementation for numerically solving the transit dynamics of red blood through splenic slits

## II. PROBLEM DESCRIPTION AND MATHEMATICAL FORMULATION

Let us consider a droplet of volume  $V_d$  with a viscosity  $\eta_d$  in an external fluid with a viscosity  $\eta_o$  passing through a circular pore of radius r and finite length L [Fig. 1(a)]. The whole process is divided into five stages as shown in Fig. 1(a) by following the convention in Zhang  $et\ al.^{29}$  We define the volume  $v_{\rm II}$  as the volume of the droplet, which has passed the pore entrance. We ignore the transit time of stages I and V as described in the aforementioned study,  $^{29}$  since in our case, it is much shorter compared to other stages II–IV shown in Fig. 1 (a). We also assume that the initial droplet radius  $R_d$  is larger than the pore radius:  $R_d > r$ .

#### A. Pressure drops

We aim to calculate the total transit time when the prescribed pressure drop  $\Delta P = P1 - P7$  is constant during the transit process, as shown in Fig. 1(b). The total pressure drop between the two sides along the red path in Fig. 1(b) can be grouped into four terms as follows:

$$\Delta P = P1 - P7 = \Delta P_{\text{mem}} + \Delta P_{\text{poise},\eta_d} + \Delta P_{\text{poise},\eta_0} + \Delta P_{\text{sampson}}, \quad (1)$$
 where the first term,

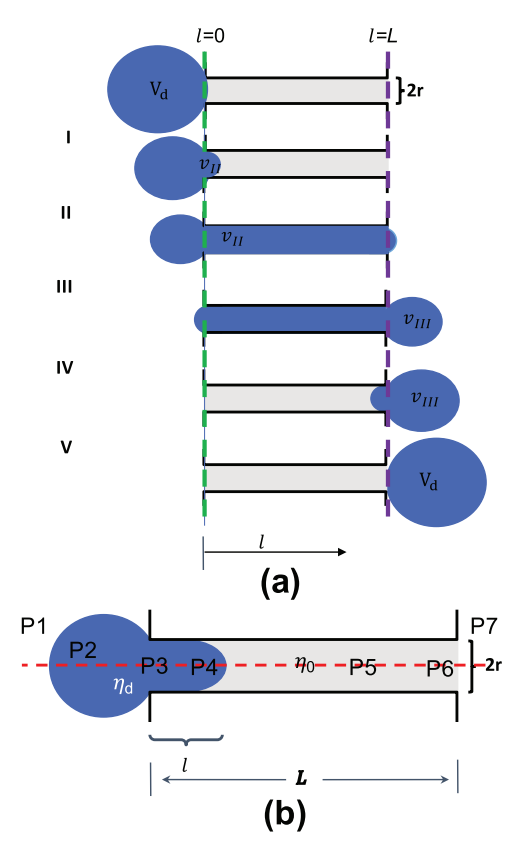


**FIG. 1.** Sketch of the problem of a droplet of volume  $V_d$  passing through a narrow circular pore of radius r and length L. The volume of the droplet passing the entrance (l=0), that is, the volume in the right hand side of the green dashed line, is defined as  $v_{\rm II}$ . The volume of the droplet passing the exit (l=L), that is, the volume in the right hand side of the purple dashed line, is defined as  $v_{\rm III}$ . (a) Stages of the droplet passage through the pore. Stage I is a short process of developing a hemisphere at the pore entrance with a radius of r. Stage II ends when the volume  $v_{\rm II} = L\pi r^2 + 2/3\pi r^3$ . Stage III ends when  $v_{\rm II} = V_d - 2/3\pi r^3$ . Stage IV ends when  $v_{\rm III} = V_d - 2/3\pi r^3$ . Stage V is the short process of the hemisphere before the pore exit retracting to the radius of the spherical droplet. (b) Dimensions of the studied system (pore and droplet dimensions), viscosities  $\eta_d$  and  $\eta_o$  of the droplet and external fluid, respectively, and pressures outside and along the droplet/pore (P1—P7).

$$\Delta P_{\text{mem}} = P1 - P2 + P4 - P5 = 2\sigma(1/R_R - 1/R_L), \qquad (2)$$

is the pressure term corresponding to pressure drops across the droplet membrane, induced by the membrane surface tension  $\sigma$ , which can be calculated using the Young–Laplace equation on both sides of the droplet.  $R_R$  and  $R_L$  are the right and left radii of the deformed droplet, respectively.

The second term,

$$\Delta P_{\text{poise},\eta_{\text{d}}} = P3 - P4 = \frac{4\eta_d (V_{\text{max}} - V_{\text{int}})l}{(r - h)^2},$$
 (3)

is the Poiseuille-related pressure drop in the cylindrical part of the droplet inside the pore, of length l, where  $V_{\rm max}$  is the maximum velocity and  $V_{\rm int}$  is the velocity of the interface between the droplet and the lubrication layer, and h is the thickness of the lubrication layer as shown in Fig. 2.

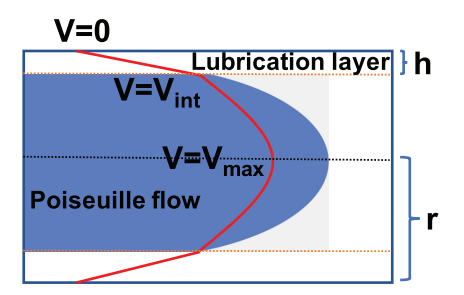


**FIG. 2.** Velocity profile inside the pore with a lubrication layer between the droplet and the pore wall.

The third term.

$$\Delta P_{\text{poise},\eta_0} = P5 - P6 = \frac{Q \times 8\eta_0(L-l)}{\pi r^4},$$
 (4)

is the Poiseuille-related pressure drop in the region of the pore where there is only an exterior fluid, and *Q* is the flow rate.

The fourth term,

$$\Delta P_{\text{Sampson}} = P2 - P3 + P6 - P7 = \frac{Q_1 \times 3\frac{\eta_d}{2}}{(r-h)^3} + \frac{Q \times 3\frac{\eta_0}{2}}{r^3}, \quad (5)$$

is the Sampson flow term of a flow passing through an infinitely thin circular hole<sup>40</sup> and  $Q_1$  is the flow rate of the droplet part only. Since the original Sampson flow is about a single-phase flow, we divide our problem into two half problems with two different viscosities,  $\eta_d$  for the droplet and  $\eta_o$  for the exterior fluid, and add a factor of 1/2 for each. This factor of 1/2 is validated by simulating the two-phase flows with different viscosities in the case of Sampson as shown in Fig. 8 in the Appendix. The simulation results show that it is reasonable to divide it to two half problems. However, this approximation might lead to a significant error if the droplet diameter is only slightly larger than the tube diameter because the original Sampson flow is a solution of an infinite space while the half problem of the droplet only covers finite space near the pore, although most of the pressure drop occurs near the pore. In addition, the original Sampson solution assumes a pore in a sheet with zero thickness, while the edges are rounded in both experimental and computational data used in this study, which give finite thickness [Fig. 8(a)] and can introduce additional error. In the literature, it has been shown that the flow in Fig. 1 can be approximated well by a combination of Sampson and Poiseuille flows.

#### B. Lubrication layer, velocity profile, and flow rate

The lubrication theories by Bretherton,<sup>34</sup> Secomb *et al.*,<sup>36</sup> and Bruinsma<sup>35</sup> showed that the thickness of the lubrication layer is inversely proportional to the tension in the membrane of the bubble, the droplet, the vesicle or red blood cell membranes, which is given as follows:<sup>35</sup>

$$h(V_{\text{int}}) = 2.05r(\eta_0 V_{\text{int}}/\sigma)^{2/3} = 2.05r(Ca)^{2/3},$$
 (6)

where  $V_{\rm int}$  is the velocity of the interface shown in Fig. 2 and  $Ca = \eta_0 V_{\rm int}/\sigma$  is the capillary number. To calculate the flow rate in the pore, we first calculate the velocity profile of the cylindrical part of the droplet based on the continuity of the fluid shear stress across the interface of the droplet, i.e., the shear stress  $\tau_1 = \frac{\eta_0 V_{\rm int}}{\hbar}$  from the side of

the lubrication layer should be equal to the shear stress  $au_2 = \frac{2\eta_d(V_{max} - V_{int})}{r - h}$  from the droplet Poiseuille flow side  $au_1 = au_2$ , leading to

$$\frac{\eta_0 V_{\text{int}}}{h} = \frac{2\eta_d (V_{\text{max}} - V_{\text{int}})}{r - h}.$$
 (7)

Note that a 2D Poiseuille flow has a parabolic velocity profile and has the maximum slope or shear stress at the interface. Note that h is also a function of  $V_{\rm int}$  as shown in Eq. (6), so that this is a nonlinear equation of  $V_{\rm int}$  for a given  $V_{\rm max}$ ,  $\sigma$ , and r.

We can define

$$\alpha = \frac{V_{\text{max}} - V_{\text{int}}}{V_{\text{max}}} = \frac{\eta_0(r - h)}{\eta_0(r - h) + 2\eta_d h},$$
 (8)

so that  $V_{\rm int}=(1-\alpha)V_{\rm max}.$  Note that  $\alpha=1$  for the ideal Poiseuille flow and  $\alpha=0$  for the ideal plug flow.

The flow rate of the entire cross section includes the flow rate in the Poiseuille flow part  $(Q_1)$  and the flow rate in the lubrication layer part  $(Q_2)$ , giving the total flow rate as follows:

$$Q = Q_1 + Q_2 = \int_0^{r-h} V_{\text{avel}} \, dA + \int_{r-h}^r \frac{r - \rho}{h} V_{\text{int}} \, dA,$$

where  $\rho$  is the radial co-ordinate of the polar co-ordinate system and r is the tube radius and  $dA = 2\pi \rho d\rho$ . Since the average velocity in a 3D tube Poiseuille flow is half the maximum velocity, the average velocity of the Poiseuille flow part is given as follows:

$$V_{\text{avel}} = (V_{\text{max}} - V_{\text{int}})/2 + V_{\text{int}} = (V_{\text{max}} + V_{\text{int}})/2.$$

Thus,

$$Q_1 = V_{\text{avel}} \pi (r - h)^2 = \frac{\pi (r - h)^2 (V_{\text{max}} + V_{\text{int}})}{2}.$$
 (9)

For the lubrication layer, the flow rate

$$Q_2 = \int_{r-h}^{r} \frac{r - \rho}{h} V_{\text{int}} 2\pi \rho \, d\rho = \frac{\pi h (3r - 2h) V_{\text{int}}}{3}. \tag{10}$$

Then, the total flow rate is given as follows:

$$Q = Q_1 + Q_2 = \frac{\pi (r - h)^2 (V_{\text{max}} + V_{\text{int}})}{2} + \frac{\pi h (3r - 2h) V_{\text{int}}}{3}$$

$$\approx \frac{\pi r^2 (V_{\text{max}} + V_{\text{int}})}{2}.$$
(11)

Note that typically  $Q_1 \gg Q_2$  because  $r \gg h$ , and  $Q \approx \frac{\pi r^2 (V_{max} + V_{int})}{2}$ .

Since the flow rate is the same for every cross section due to mass conservation, the total pressure drop is given as follows:

$$\Delta P = 2\sigma (1/R_R - 1/R_L) + \frac{(V_{\text{max}} - V_{\text{int}}) \times 4\eta_d l}{(r - h)^2} + \frac{Q \times 8\eta_0 (L - l)}{\pi r^4} + \frac{Q \times 8\eta_0 (L - l)}{\pi r^4} + \frac{Q_1 \times 3\frac{\eta_d}{2}}{(r - h)^3} + \frac{Q \times 3\frac{\eta_0}{2}}{r^3}.$$
(12)

If assuming  $\frac{Q_1}{(r-h)^3} \approx \frac{Q}{r^3}$  It can be simplified as

$$\Delta P = 2\sigma (1/R_R - 1/R_L) + \frac{(V_{\text{max}} - V_{\text{int}}) \times 4\eta_d l}{(r - h)^2} + \frac{Q \times 8\eta_0 (L - l)}{\pi r^4} + \frac{Q \times 3\frac{\eta_0 + \eta_d}{2}}{r^3}.$$
(13)

Since all variables in Eq. (12) or (13) are either constants or functions of  $V_{\rm max}$ , given a prescribed pressure drop  $\Delta P$ , Eq. (12) or (13) can be used to solve for  $V_{\rm max}$  using a nonlinear solver. Note that h is also a function of  $V_{\rm max}$  or  $V_{\rm int}$  as shown in Eqs. (6) and (8).

In summary, we make the following assumptions in our model. First, we assume that the droplet is larger than the pore in terms of volume so that it can fill the pore entirely. Second, we assume the capillary number is low enough that the droplet would not breakup during the process. Third, the droplet has a constant surface tension and the interior and exterior fluid behaviors as Newtonian fluids with different viscosities. Fourth, the Reynold number remains low that the flow is characterized as a creeping (Stokes) flow. Fifth, the flow field is approximated by a combination of Sampson flow (two half problems with different viscosities as justified in Fig. 8 in the Appendix) and a Poiseuille flow with lubrication layers.

#### C. Transit time

Based on the pressure drops of the different stages, we will derive the equations for estimating the stage transit times and total transit time.

#### 1. Stage II

We denote the average velocity of the droplet front moving in the pore in stage II as  $\overline{U}_2(l) = V_{\rm int}$ , and the pressure due to viscous force inside the pore is given by Eq. (12) with

$$R_L = \left[ \left( V_d - l\pi r^2 - 2/3\pi r^3 \right) / (4\pi/3) \right]^{1/3}, \quad R_R = r,$$
 (14)

where l is defined as the length of the cylindrical part of the droplet inside the pore, r is the tube radius, and  $V_d$  is the droplet volume. The time evolution of l can be written as a nonlinear ODE as follows:

$$\frac{dl}{dt} = V_{\text{int}}(l). \tag{15}$$

We can numerically integrate this ODE from t=0 with an initial condition of l(t=0)=0 to an unknown time  $t_2$  to reach  $l(t_2)=L$ . This unknown time  $t_2$  can then be solved numerically. If the surface tension  $\sigma$  is negligible or is constant only on the left side, Eq. (15) can be integrated to get the closed-form solutions shown later. However, in some cases,  $l(t_2)=L$  is not a good criterion to mark the end of stage II because the flow in the tube center moves much faster than the flow near the lubrication layer  $(V_{\rm max}\gg V_{\rm int})$ . When l calculated based on the integration of  $V_{\rm int}(l)$  reaches L, the part of the droplet in the tube center has already moved far away. Instead, we use  $\nu_{\rm II}$ , the volume of the droplet passing through the entrance (volume on the right hand side of the green dashed line in Fig. 1) as the criterion to end stage II. When  $\nu$  equals  $L\pi r^2 + 2/3\pi r^3$ , stage II ends.

#### 2. Stage III

Let  $v_{\text{III}}$  denote the volume of the right sphere (volume on the right hand side of the purple dashed line in Fig. 1). The pressure drop is given as follows:

$$\Delta P = 2\sigma (1/R_R - 1/R_L) + \frac{(V_{\text{max}} - V_{\text{int}}) \times 4\eta_d L}{(r - h)^2} + \frac{Q_1 \times 3\frac{\eta_d}{2}}{(r - h)^3} + \frac{Q \times 3\frac{\eta_0}{2}}{r^3},$$
(16)

where  $R_R = [\nu_{\rm III}/(4\pi/3)]^{1/3}$  and  $R_L = [(V_d - L\pi r^2 - \nu_{\rm III})/(4\pi/3)]^{1/3}$ . However, special care is required for  $R_R < r$  or  $R_L < r$  since it generated an unphysical large pressure jump; therefore, we apply that if  $R_R < r$ , then  $R_R = r$ , and the same for  $R_L$  The time evolution of  $\nu$  can be written as a nonlinear ODE as follows:

$$\frac{dv_{\text{III}}}{dt} = Q(v_{\text{III}}). \tag{17}$$

For this ODE of  $v_{\rm III}(t)$ , with initial condition  $v_{\rm III}(0) = 2\pi r^3/3$ , we solve for  $t_3$  numerically so that  $v_{\rm III}(t_3) = V_d - L\pi r^2 - 2\pi r^3/3$ .

#### 3. Stage IV

The pressure drop for the droplet in stage IV is represented as follows:

$$\Delta P = 2\sigma (1/R_R - 1/R_L) + \frac{(V_{\text{max}} - V_{\text{int}}) \times 4\eta_d (L - l)}{(r - h)^2} + \frac{Q \times 8\eta_0 l}{\pi r^4} + \frac{Q_1 \times 3\frac{\eta_d}{2}}{(r - h)^3} + \frac{Q \times 3\frac{\eta_0}{2}}{r^3},$$
(18)

where  $R_L = r$  and  $R_R = [(V_d - l\pi r^2 - 2/3\pi r^3)/(4\pi/3)]^{1/3}$ .

This is a nonlinear ODE of l. We can numerically integrate this ODE from t=0 with an initial condition of l(t=0)=L to an unknown time  $t_4$  to reach  $l(t_4)=0$ . This unknown time  $t_4$  then can be solved numerically.

If we denote l = L - l', then we have

$$\Delta P = 2\sigma (1/R_R - 1/R_L) + \frac{(V_{\text{max}} - V_{\text{int}}) \times 4\eta_d l'}{(r - h)^2} + \frac{Q \times 8\eta_0 (L - l')}{\pi r^4} + \frac{Q_1 \times 3\frac{\eta_d}{2}}{(r - h)^3} + \frac{Q \times 3\frac{\eta_0}{2}}{r^3}.$$
 (19)

This is a nonlinear ODE of l. We can numerically integrate this ODE from t=0 with an initial condition of l (t=0)=0 to reach l  $(t_4)=L$ . This unknown time  $t_4$  then can be solved numerically.

Finally, the total transit time is given as follows:

$$t_T = t_2 + t_3 + t_4. (20)$$

#### D. Critical pressure and surface tensions

The critical pressure is the total pressure drop necessary for a droplet to squeeze through a pore. If the total pressure drop  $\Delta P \leq \Delta P_{\rm mem}$  at the beginning of stage II, where  $R_{\rm R}$  is smallest and  $R_{\rm L}$  is largest, then the droplet will not pass through the pore. The critical pressure is determined by the pore radius r, the droplet volume  $V_d$ , and the surface tension  $\sigma$ . For a circular pore, the critical pressure is given by the expression

$$P_c = 2\sigma \left\{ 1/r - \left[ \left( \left( V_d - (2\pi r^3)/3 \right) \right) / (4\pi/3) \right]^{-\frac{1}{3}} \right\}.$$
 (21)

Similarly, we can define the critical surface tension for a droplet to pass under a given pressure drop  $\Delta P$  as follows:

$$\sigma_c = \frac{\frac{1}{2}\Delta P}{1/r - \left[\left(\left(V_d - (2\pi r^3)/3\right)\right)/(4\pi/3)\right]^{-\frac{1}{3}}}.$$
 (22)

## E. Procedure to obtain numerical solutions for finite surface tension cases

While an analytical solution can be found when the surface tension term  $\Delta P_{\rm mem}$  is absent, the differential equations in the above sections cannot be integrated manually when the surface tension of both the right and left spheres are considered. In order to find transit time when the surface tension is nonzero, we used the ODE solvers ode45 and ode23. In cases where ode45 failed to integrate an equation, ode23 was used to generate the figures in our study. We also applied the event function to calculate the transit time when certain conditions are met, such as  $l(t_2) = L$  in Eq. (15).

#### III. RESULTS

In the following, we will first derive the closed-form solution of the transit time for a simplified theory of a wetting droplet with small surface tension. Then, we will validate the numerical solution of the general theory with finite surface tension and lubrication layer thickness against the experimental result and the numerical result by solving the full problem using the finite element method (FEM) with the phase-field method. After validations, we will study the effects of pressure, droplet viscosity, droplet dimension, pore dimension, and surface tension on transit time.

## A. Closed-form solution for a circular pore for highly viscous droplets

In certain situations when the droplet wets the wall, and the surface tension is low that its contribution to pressure drop is much smaller than the Poiseuille term, we can obtain a closed-form solution of the transit time under these additional assumptions besides the general assumptions listed above. For example, consider a droplet with a radius of 5  $\mu$ m with a surface tension of 35 pN/ $\mu$ m and an inner viscosity of 400 Pa s under a pressure drop of 2000 Pa to pass a pore with a radius of 2.0  $\mu$ m and a length of 6.0  $\mu$ m. The maximum pressure drop due to surface tension is about 35 Pa, which is much smaller than the total pressure drop of 2000 Pa.

#### 1. Stages II and IV

For wetting droplets with small surface tension, Eq. (14) becomes the following equation:

$$\Delta P = \frac{V_{\text{max}} \times 8\eta_d l}{r^2} + \frac{V_{\text{max}} \times 8\eta_0 (L - l)}{r^2} + \frac{V_{\text{max}} \times 3\pi \frac{\eta_0 + \eta_d}{2}}{r^3}, \quad (23)$$

which can be solved analytically. If we let  $a=\frac{8(\eta_d-\eta_0)}{r^2}$  and  $b=\frac{8\eta_0L}{r^2}+\frac{3\pi^{(\eta_d+\eta_0)}}{r}$ , the above equation can be rewritten as follows:

$$\frac{dl}{dt} = V_{\text{max}} = \frac{\Delta P}{a \times l + b}.$$
 (24)

Separating the variables and integrating leads to

$$\int dl(a \cdot l + b) = \int \Delta P \, dt,$$
  
$$\frac{1}{2}al^2 + b \cdot l = \Delta P \cdot t + c.$$

With boundary conditions of

$$l = 0 \quad \text{at} \quad t = 0 : c = 0,$$

$$l = L \quad \text{at} \quad t_{2//4} \quad \frac{1}{2}aL^{2} + b \cdot L = \Delta P \cdot t_{2//4},$$

$$t_{2//4} = \frac{\frac{1}{2}aL^{2} + bL}{\Delta P},$$

$$t_{2//4} = \frac{4(\eta_{d} - \eta_{0})}{r^{2}}L^{2} + \left(\frac{8\eta_{0}L}{r^{2}} + 3\pi\frac{\frac{(\eta_{d} + \eta_{0})}{2}}{r}\right)L$$

$$\Delta P \qquad (25)$$

is the transition time for stage II or IV.

#### 2. Stage III

For wetting droplets with small surface tension,

$$v = \frac{\Delta P \cdot t}{8\eta_d L} + \frac{3\eta_d}{r^3} + V_0.$$
 (26)

With the initial condition that  $v(0) = V_0 = \frac{2\pi r^3}{2}$ ,

$$v(t_3) = \frac{\Delta P}{\frac{8\eta_d L}{\pi r^4} + \frac{3\eta_d}{r^3}} t_3 + V_0 = V_d - L \cdot \pi r^2 - \frac{2\pi r^3}{3} ,$$

$$t_3 = \frac{\left(V_d - L \cdot \pi r^2 - \frac{4\pi r^3}{3}\right)}{\Delta P} \left(\frac{8\eta_d L}{\pi r^4} + \frac{3\eta_d}{r^3}\right).$$
(2)

Finally, the total transit time

$$\begin{split} t_T &\cong t_2 + t_3 \! + \! t_4 \\ &= \frac{2 \! \left[ \frac{4 (\eta_d - \eta_0) L^2}{r^2} \! + \! \left( \frac{8 \eta_0 L}{r^2} \! + \! 3 \pi \frac{\frac{(\eta_d \! + \! \eta_0)}{2}}{r} \right) \! L \right]}{\Delta P} \\ &\quad + \frac{\left( V_d \! - \! L \cdot \! \pi r^2 \! - \! \frac{4 \pi r^3}{3} \right)}{\Delta P} \! \left( \frac{8 \eta_d L}{\pi r^4} \! + \! \frac{3 \eta_d}{r^3} \right). \end{split}$$

#### 3. Dimensional analysis and scaling

In the limiting case when stage III is dominant and stages II and IV can be ignored, for example, L is very small, and the droplet radius is much larger than the tube radius, i.e.,  $R\gg r$ , then Eq. (28) becomes

$$t_{T} = \frac{\frac{4\pi R^{3}}{3}}{\frac{3}{\Delta P}} \left( \frac{8\eta_{d}L}{\pi r^{4}} + \frac{3\eta_{d}}{r^{3}} \right). \tag{29}$$

We can normalize the transit time by a dimensionless parameter as  $\pi_1 = \frac{\Delta P \, t_T}{\eta_d}$  and the geometry of the problem by two dimensionless parameters as  $\pi_2 = \frac{R}{r}$ ,  $\pi_3 = \frac{L}{r}$ ; then, Eq. (29) can be written as

$$\pi_1 = \frac{4\pi}{3} \left( \frac{8\pi_2^3 \pi_3}{\pi} + 3\pi_2^3 \right) = \frac{4\pi}{3} \pi_2^3 \left( \frac{8\pi_3}{\pi} + 3 \right). \tag{30}$$

#### 4. Case of finite surface tension

With finite surface tension, we can define another dimensionless parameter as follows:

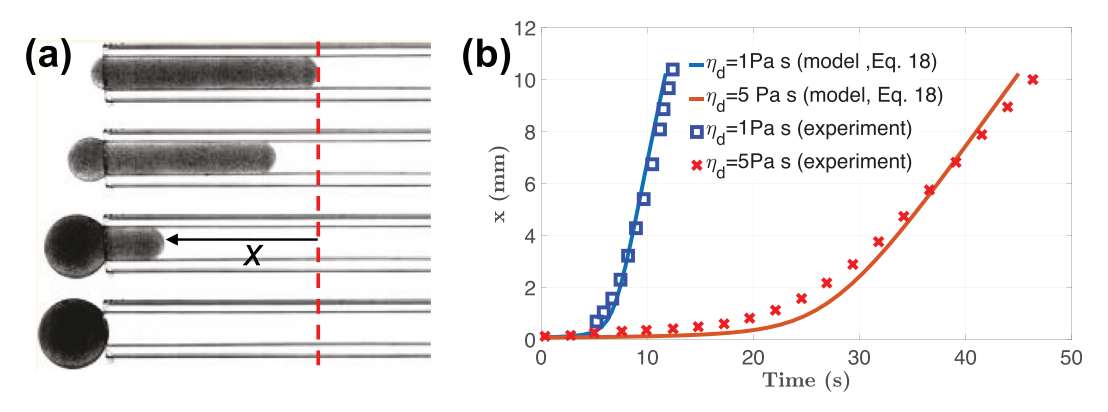
$$egin{aligned} \pi_4 &= rac{\sigma}{\sigma_c} = rac{\sigma}{0.5 \, \Delta P \Big/ \Big\{ 1/r - ig[ ig( (V_d - (2\pi r^3)/3) ig)/(4\pi/3) ig]^{-rac{1}{3}} \Big\}} \ &pprox rac{2\sigma \{ 1/r - 1/R \}}{\Delta P}. \end{aligned}$$

 $\pi_4\approx\frac{2\sigma}{\Delta P\,r}$  if  $r\!\ll\!R.$  In general cases with surface tension and lubrication, we expect

$$\pi_1 = f(\pi_2, \, \pi_3, \pi_4).$$
(31)

#### B. Validation of theory against experiments

We first validated our theory against the experiment of capillary extraction of a droplet with a higher viscosity than the surrounding fluid conducted by Piroird  $et\ al.^{42}$  as shown in Fig. 3(a). A nonwetting droplet slug placed at the end of a capillary tube is unstable, and a small displacement results in the complete extraction of the liquid from the tube. In the experiment, the length of the droplet inside the tube x was recorded as a function of time. We applied our theory to



(28)

FIG. 3. Validation of the theory against experiments. (a) The snapshots of the droplet during the exiting process. Adapted from the experimental observation by Piroird *et al.* Langmuir **27**, 9396 (2011). (b) Comparison of the exiting dynamics of a droplet against the experiment. 42

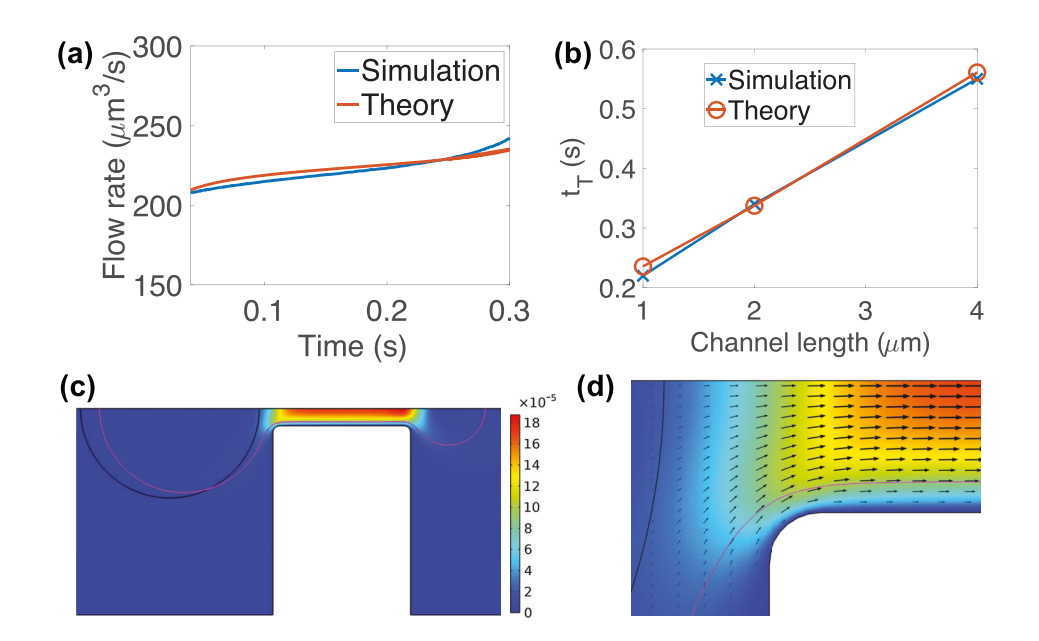


**FIG. 4.** Validation of the theory against FEM simulations. (a) Comparison of the flow rate between theory and FEM in the case of a pore length of  $4\,\mu\text{m}$ . (b) Comparison of the total transit time between theory and FEM simulation. (c) Velocity field (m/s) in the FEM simulation in the case of a pore length of  $4\,\mu\text{m}$ . (d) Zoom-in of the flow field near the entrance in panel (c).

model this process by solving Eq. (18), which only involves stage IV. The surface tension  $\gamma$  between oil and the water ethanol mixture used in the experiment is  $20\,\mathrm{mN/m}=20\,000\,\mathrm{pN/\mu m}$ . The glass tube has a radius Ro = 0.88 mm, and the droplet has a radius of 2 mm. We compared our theoretical results with the experiments with two different droplet viscosities. Figure 3(b) shows that our theory matches excellently with the experimental measurements for both cases. The lubrication layer thickness h is on the order of 1  $\mu$ m, which can be calculated from Eq. (7) with  $V_{\rm int}=0.9\,V_{\rm max}$  estimated from the experiment so that  $h\approx \frac{\eta_0 V_{\rm int} R_o}{2\eta_d (V_{\rm max}-V_{\rm int})} = \frac{9\times 0.001\,\mathrm{Pa}\,\mathrm{s}\times 880\,\mu\mathrm{m}}{2\times 5\,\mathrm{Pa}\,\mathrm{s}} = 0.792\,\mu\mathrm{m}.$ 

#### C. Validation of theory against FEM simulations

We also validated our theory by comparing the results with full finite element simulations by COMSOL.<sup>43</sup> In this case, we used a circular pore with a finite length of  $4 \mu m$  and a radius of  $0.5 \mu m$ . In COMSOL, the axisymmetric geometry is used, and the phase-field method is applied to simulate the two-phase flows of a nonwetting droplet with finite surface tension. A droplet of an initial radius of 2.6  $\mu$ m and a surface tension of 10 pN/ $\mu$ m, much lower than the droplet slug studied by Piroird et al. above, 42 is used and a pressure drop of 100 Pa between the inlet and the outlet is applied. The inner viscosity is 0.012 Pa s and the exterior viscosity is 0.0012 Pa s. Figure 4(a) shows the flow rate as a function of time predicted by our theory and the FEM simulation, and they match well. In addition, we compare the transit time of the droplet through the pores with different pore lengths in Fig. 4(b). With a wide range of 1–4  $\mu$ m, the theoretical predictions are in good agreement with the numerical predictions. In Figs. 4(c) and 4(d), we also plot the velocity fields in the FEM simulations at a specific time snapshot. The flow field near the entrance is close to a superposition of the Sampson and the Poiseuille flow as shown before by others.<sup>41</sup> The lubrication layer thickness h predicted from the theory is on the order of 0.1  $\mu$ m, which is consistent with the COMSOL numerical simulation [Fig. 4(d)].

Based on the definition of stages in Fig. 1, the simulations of the case with a pore length of  $4\,\mu m$  in Fig. 4 show that stage I takes about 0.002 s, stage II takes 0.028 s, stage III takes 0.522 s, stage IV takes 0.012 s, and stage V takes about 0.001 s. By comparison, our theoretical model predicts that stage II takes 0.0312 s, stage III takes 0.528 s, and stage IV takes 0.0118 s, while assuming stages I and V take almost no time. These results show that our theory and its assumptions are quite consistent with the numerical simulations.

For COMSOL simulation, due to the symmetry, we simulated the process as an unsteady 2D axisymmetric problem. We used 347 494 triangular elements (186 393 degrees of freedom) and refined mesh near the boundary to resolve the lubrication layer. An automatic time stepping using an implicit backward differentiation formula (BDF) solver is applied to solve this unsteady problem. Phase-field method is used to track the interface between two phases of fluids with constant surface tension. Our results showed that the FEM simulations are converged with respect to the number of element and time step. Multiphysics coupling between the fluid flow solver (algebraic multigrid, AMG) and phase field solver (direct sparse solver based on PARDISO) is achieved in a segregate way.

### D. Effects of pressure and drop viscosity on transit time

To analyze the time taken for a droplet to squeeze through a circular pore, we studied the effect of the total pressure drop  $\Delta P$ , surface tension  $\sigma$ , pore length L, radius r, droplet volume  $V_d$ , and viscosity  $\eta_d$ . We investigated the effects of each of these variables on the total transit time  $t_T$  or the inverse transit time  $1/t_T$ . In our study, we used a standard case with a pressure drop of 400 Pa, a pore length of  $2 \mu m$ , a pore radius of  $0.5 \mu m$ , a droplet volume of  $95 \mu m^3$ , a droplet viscosity of  $0.006 \, \mathrm{Pa} \, \mathrm{s}$ , and a solution viscosity of  $0.0012 \, \mathrm{Pa} \, \mathrm{s}$ . These values for droplet properties were chosen as similar to those of a typical red blood cell. We also studied the surface tension on the order of  $200 \, \mathrm{pN}/\mu m$  because this is a typical value a red blood cell can experience when

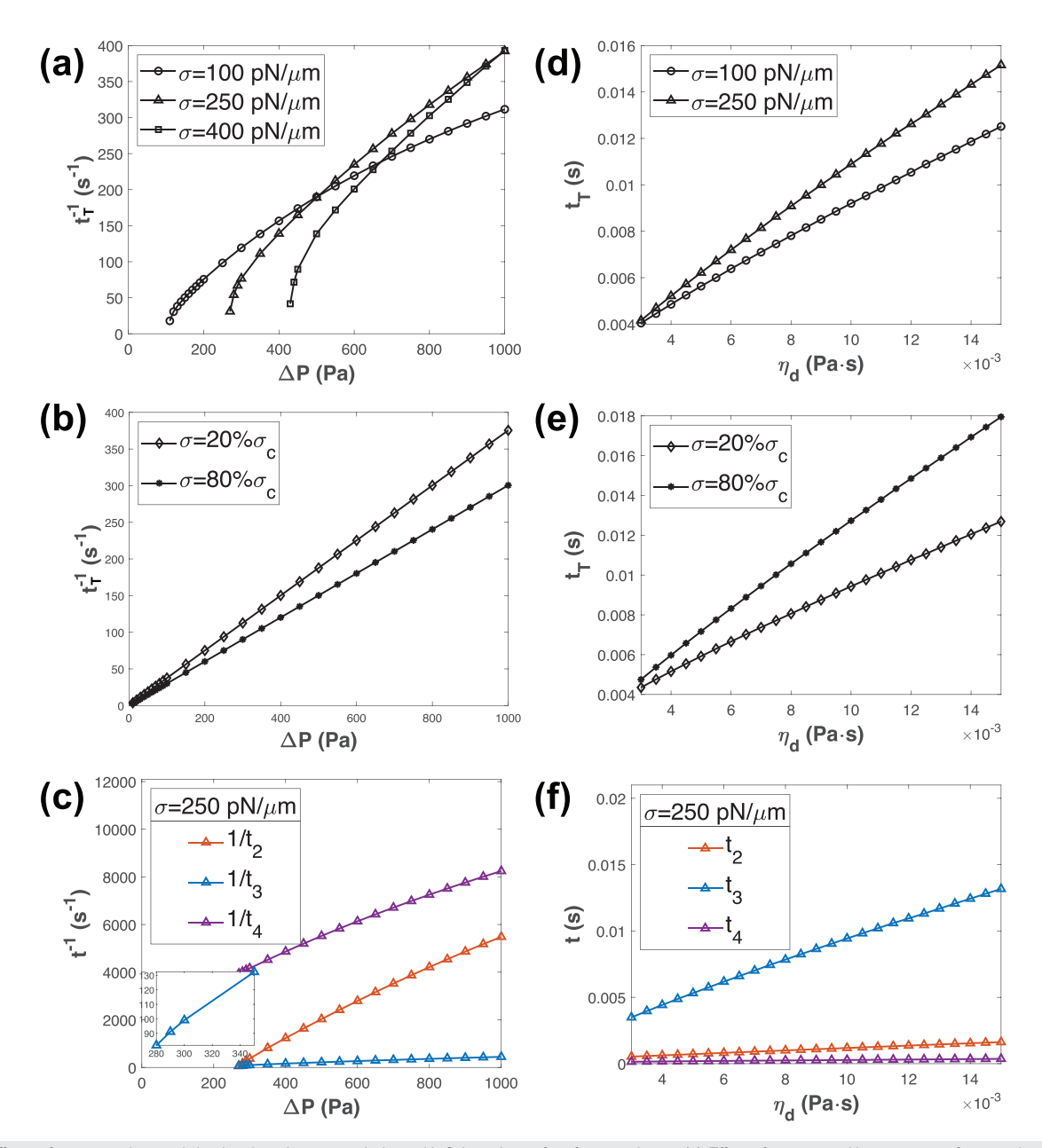


**FIG. 5.** Effects of pressure drop and droplet viscosity on transit time with finite values of surface tension  $\sigma$ . (a) Effect of pressure with constant surface tension values. (b) Effect of pressure drop with fixed surface tension percentage to critical surface tension. (c) Effect of pressure drop on transit times of different stages. (d) Effect of droplet viscosity with constant surface tension values. (e) Effect of droplet viscosity with fixed surface tension percentage to critical surface tension. (f) Effect of droplet viscosity on transit times of different stages.

passing through the slit in the spleen, <sup>9,44</sup> while the lysing tension of the bilayer is about 10–20 mN/m. <sup>45</sup> Using these values as a baseline, the effect of each variable on transit time was investigated.

In all FEM simulations with the phase-field method we conducted, we did not observe any breakup of the droplets. In the literature, it has been shown that for droplets in straight tubes, the critical capillary number for a droplet to breakup is above 1.5.46,47 The critical capillary number can be lower in the case of droplets passing through

narrow constriction rather than a straight tube, but we have the capillary number below 0.5 for all of our cases studied.

For surface tensions of 100, 250, and 400 pN/ $\mu$ m, the inverse transit time in 1/s was obtained for pressure drops from 1000 Pa down to the approximate critical pressure, as shown in Fig. 5(a). The pressure–time curves for all surface tensions are approximately linear at higher pressure drops, above around 700 Pa. However, below that pressure drop, there appears to be a downward curvature until the

critical pressure is reached. The relationship between the inverse transit times of the surface tensions also changes as pressure drop increases. For example, the  $100 \, \mathrm{pN}/\mu\mathrm{m}$  droplet having the highest relative 1/transit time at lower pressure drops, before dropping to having the lowest 1/transit time compared to other surface tensions.

An inverse transit time in 1/s was obtained for pressure drops ranging from 10 to 1000 Pa at 20% and 80% of the critical surface tension of each point. A higher percentage of the critical surface tension resulted in a longer transit time compared to lower percentages. However, in both cases, there was a linear relationship between pressure drop and time, as seen in Fig. 5(b). This can be explained in the following analysis.

By plugging  $Q \approx Q_1 \approx \frac{\pi r^2 (V_{\text{max}} + V_{\text{int}})}{2}$  into Eq. (16), we get

$$\begin{split} \Delta P &\approx 2\sigma (1/R_R - 1/R_L) + \frac{8Q\eta_d L}{\pi r^4} - \frac{8V_{\text{int}} \times \eta_d L}{r^2} + \frac{Q \times 3\frac{\eta_d}{2}}{r^3} \\ &+ \frac{Q \times 3\frac{\eta_0}{2}}{r^3}. \end{split} \tag{32}$$

If we assume that both surface tension and interface velocity are linearly proportional to pressure drop  $\sigma = c_1 \Delta P$  and  $V_{int} = c_2 \Delta P$ , where  $c_1$  and  $c_2$  are constants, we have

$$Q = \frac{dv}{dt}$$

$$= \frac{\Delta P \left[ 1 - 2c_1 (4/3\pi)^{1/3} \left( 1/v^{1/3} - 1/(V_c - L\pi r^2 - v)^{1/3} \right) - \frac{8L\eta_d c_2}{r^2} \right]}{\frac{8\eta_d L}{\pi r^4} + \frac{3\eta_d}{2r^3} + \frac{3\eta_0}{2r^3}}$$

$$= \Delta P f(v). \tag{33}$$

Rearrange the equation and integrate it, we have

$$\int_{V_0}^{V_c} \frac{dv}{f(v)} = \Delta P \int_0^{t_T} dt = \Delta P t_T.$$
 (34)

Therefore,  $1/t_T$  is proportional to  $\Delta P$  if  $\sigma = c_1 \Delta P$  and  $V_{int} = c_2 \Delta P$ .

A 100-fold increase in the pressure drop, from 10 to 1000 Pa, corresponded with an approximately 100-fold increase in 1/transit time for both situations, with the inverse transit time going from 3.75 to  $375 \, {\rm s}^{-1}$  at a 20% critical surface tension and from 3.0 to  $300 \, {\rm s}^{-1}$  at an 80% critical surface tension. While both cases start with similar transit times at low pressures, the inverse transit time increases at a higher rate for a 20% critical surface tension, with a slope of about 0.375 Pa s, compared to a slope of about 0.3 Pa s at an 80% critical surface tension.

The effects of different pressure differentials on the inverse transit time for stages II, III, and IV at a surface tension of  $250\,\mathrm{pN}/\mu\mathrm{m}$  can be observed in Fig. 5(c). For all stages, the inverse transit time appears to have a linear relationship with pressure at higher pressure drops while also developing a downward curvature at lower pressure drops, as consistent with what was observed in Fig. 5(a). Stage III is the dominant phase of the droplet passing through a pore, with the lowest inverse transit time (and thus the highest transit time), while stage IV had the lowest relative transit time.

For droplet viscosities ranging from 0.003 to 0.015 Pa s, the transit time was obtained at constant surface tensions of 100 and  $250 \, \text{pN}/\mu\text{m}$ 

and at 20% and 80% of the critical surface tension. Figure 5(d) shows that at lower viscosities, the transit times for droplets with surface tensions of 100 and 250 pN/ $\mu$ m appear to converge, with the transit times being 4.35 and 4.75 ms, respectively. However, as viscosity increases, the transit times of droplets with higher constant surface tensions increase at a faster rate. There also appears to be a somewhat linear relationship in both cases. Similar results were found observed when the transit time was plotted against a range of droplet viscosities at a percentage of the critical surface tension, as shown in Fig. 5(e). No data were able to be collected for a constant surface tension of  $400 \text{ pN}/\mu\text{m}$ , likely because our default pressure drop of 400 Pa was below the critical pressure under those conditions. Figure 5(f) shows the relationship between droplet viscosity and transit time for stages II, III, and IV at a surface tension of 250 pN/ $\mu$ m. Once again, the total transit time was most greatly influenced by stage III, while stages II and IV made up a significantly smaller fraction.

#### E. Effect of pore and droplet dimensions

The relationship between transit time, in the form of the dimensionless variable  $\Delta P(t_T)/\eta_d$ , and the ratio between the length (L) and the radius of the pore was obtained for L/r values from 0.886 to 2.659, both at constant surface tensions and at percentages of the critical surface tension. When comparing  $\Delta P(t_T)/\eta_d$  to L/r at constant surface tensions, as shown in Fig. 6(a), there appears to be a linear relationship, potentially with a slight upward concavity. At the lowest assessed value of L/r, the transit time is slightly higher in conditions with a surface tension of  $100~\text{pN}/\mu\text{m}$ , compared to surface tensions of  $250~\text{pN}/\mu$  m, but increases at a significantly higher rate at  $250~\text{pN}/\mu\text{m}$ .

In Fig. 6(b), we see the effect of L/r on  $\Delta P(t_T)/\eta_d$  with surface tensions at 20% and 80% of the critical surface tension. Similar to conditions at constant surface tensions, there is an approximately linear relationship, with  $\Delta P(t_T)/\eta_d$  increasing at a higher rate with higher surface tensions.

The effect of pore radius on transit time with constant surface tension values is shown in Fig. 6(c), graphed in the dimensionless variables  $\Delta P(t_T)/\eta_d$  vs  $R^3/r^3$ . Transit times for  $R^3/r^3$  values ranging from 1.5 to 33.5 were determined as plotted. At lower surface tension values of 100 and 250 pN/ $\mu$ m, the droplet appears to behave similarly in terms of transit time, with transit time increasing at a slightly faster rate at 250 pN/ $\mu$ m and both having an approximately linear relationship. At 400 pN/ $\mu$ m, the droplet behavior is similar to that calculated at lower surface tension cases up to  $R^3/r^3 = 5$ , but as the droplet volume approaches the threshold set by  $P_C$ , the transit time increases sharply. Eventually, the critical pressure surpasses 400 Pa due to the increasing drop volume, and the droplet is no longer able to completely pass through the pore at  $R^3/r^3$  values higher than 12.23.

When the effect of pore radius on transit time was plotted with a fixed surface tension percentage of the critical surface tension, an approximately linear relationship could be observed between the transit time and drop radius cubed, as seen in Fig. 6(d). When the surface tension is 80% of the critical surface tension, the transit time increases at a slightly higher rate when the drop radius is smaller, with a slope of around 31 at  $R^3/r^3$  values from 1.53 to 15.28, which drops down to a slope of 28 at  $R^3/r^3$  values from 17 to 44.5. At surface tensions at 20% of the critical surface tension, there is a more distinct linear relationship, with a 30-fold increase in  $R^3/r^3$  corresponding to about a 20-fold increase in  $\Delta P(t_T)/\eta_d$ .

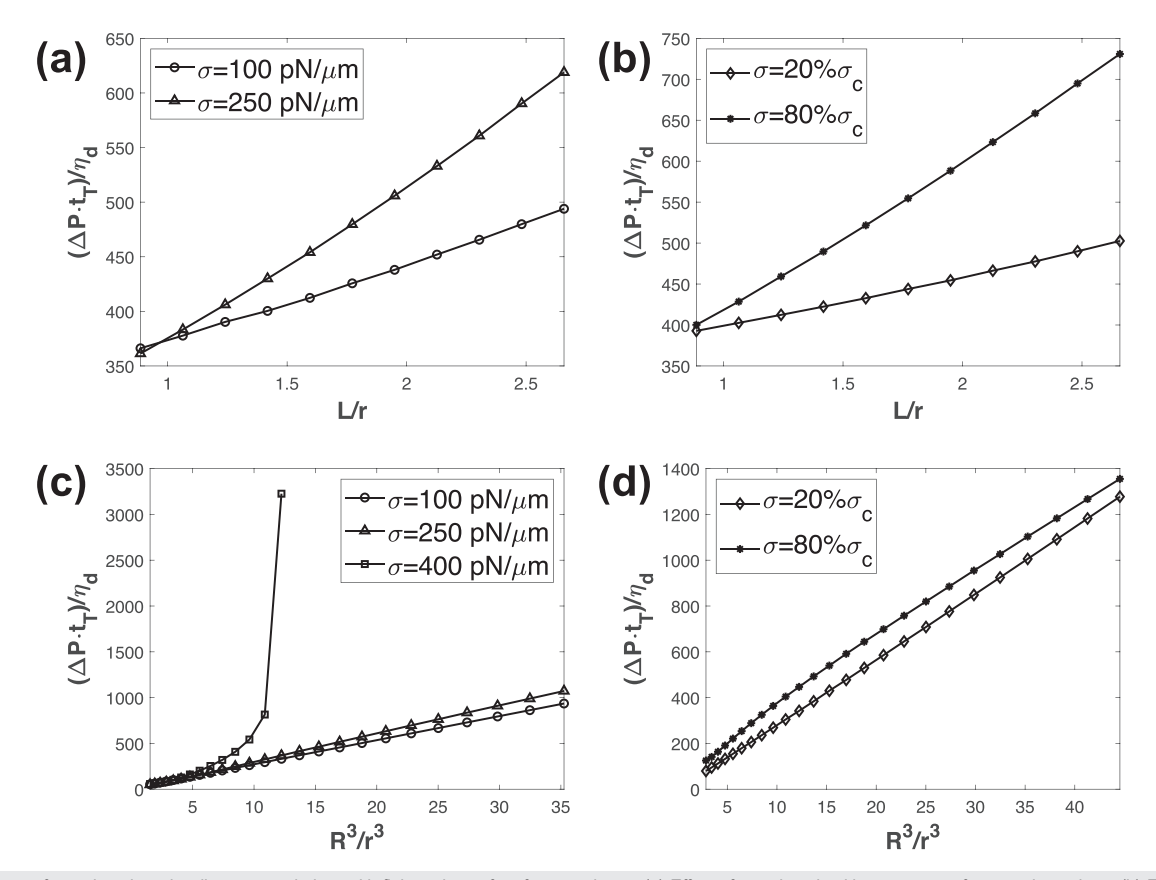


**FIG. 6.** Effects of pore length and radius on transit time with finite values of surface tension  $\sigma$ . (a) Effect of pore length with constant surface tension values. (b) Effect of pore length with fixed surface tension percentage to critical surface tension. (c) Effect of pore radius with constant surface tension values. (d) Effect of pore radius with fixed surface tension percentage to critical surface tension.

#### F. Effect of surface tension

The effect of the percentage of critical surface tension on transit time can be seen in Fig. 7(a). The transit time was obtained at surface tensions ranging from 20% to 95% of the critical surface tension. At lower percentages, there is a negative relationship between transit time and percentage of critical surface tension, but this changes to a

positive relationship starting at about 35%. From there, the transit time begins to increase exponentially as critical surface tension is approached, and it can be assumed that the droplet will not pass through the pore.

Figure 7(b) shows more detail on how stages II, III, and IV contribute to the total transit time across the same range of percent critical

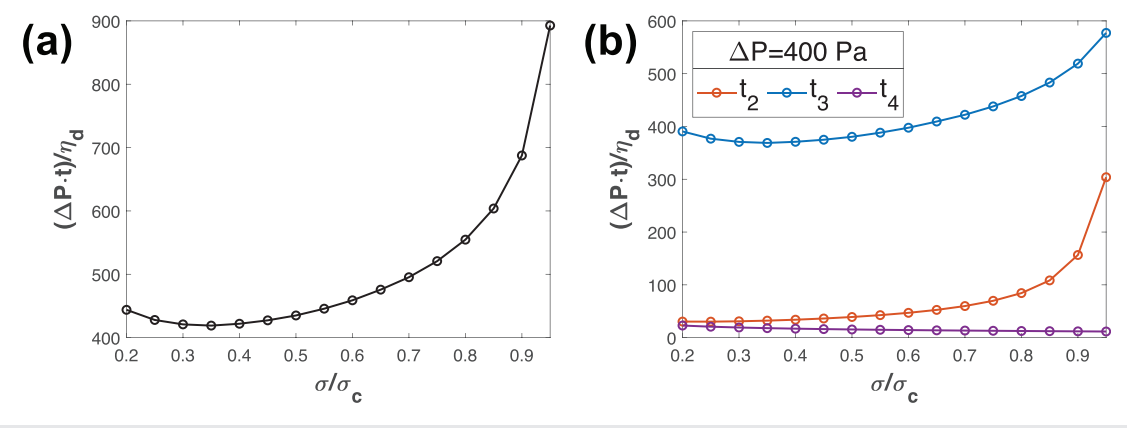


FIG. 7. Effects of the surface tension on transit time. (a) Effect of surface tension percentage on the normalized total transit time. (b) Effect of surface tension percentage on the normalized transit time of each stage under a pressure drop of 400 Pa.

surface tension. Stage III makes up the majority of the transit time and controls most of the behavior in the total transit time. However, as the critical surface tension is approached, stage II begins to increase at a much higher rate, which contributes to the sharp rise in the total transit time. Stage IV remains fairly consistent throughout all surface tensions, decreasing only slightly at a linear rate as critical surface tension is approached.

The nonmonotonic behavior observed in Fig. 7 can be explained as follows. The surface tension has two effects on the transition time. On the one hand, in stage III [Eq. (16)], the surface tension term [first term on the right hand side of Eq. (16)] resists the passage of the droplets due to the size difference of two spheres on two ends in the first half of stage III and facilitates the passage in the second half of stage III. On the other hand, the surface tension also changes the lubrication layer thickness [Eq. (6)]. For the first half of stage III until the two spheres become equal, an increased surface tension increases the resistance, therefore increasing the transit time. However, the increased surface tension also decreases the lubrication thickness h [Eq. (6)]. With a decreased h, the flow rate can be increased, therefore decreasing the transit time. These two effects of surface tension can create a nonmonotonic dependence of transit time on surface tension.

#### IV. CONCLUSION AND DISCUSSIONS

We developed an analytical theory to estimate the transit time of a droplet passing through a small circular pore with a finite length. We investigated its dependence on pressure drop, viscosity, pore dimensions, and surface tension under the creeping flow conditions. Several interesting results were found based on the theory, such as the inversely linear dependence of transit time on pressure drop when a fixed percentage of critical surface tension is applied and the nonmonotonic effect of the surface tension on transit time. This theory provides a quick and useful way to estimate the time for a droplet passing through a circular constriction and could be further developed to estimate the transit time of a vesicle or a blood cell by including specific mechanical features such as membrane bending stiffness or viscosity, etc.

While our expression evaluates the droplet volume  $v_{\rm III}$  as that of a sphere,  $v_{\rm III}$  in the beginning of stage III is actually a hemispherical cap on the right side. As a result, the expression for  $\Delta P_{\rm mem}$  appears larger and our analytical model does not perform as well when the pressure drop approaches  $P_c$ , the minimum pressure necessary for the droplet to squeeze through the circular pore. It will be more accurate to consider a spherical cup to evaluate the left and right spheres in this study; however, this will significantly increase the complexity of the analytical expressions. Because this study focused on the total transit time, and the time where the right and left caps are not approximately spherical are relatively short, our model was sufficiently accurate.

Compared to the earlier works by Zhang et al., <sup>29</sup> we replaced contributions from the contraction and expansion terms under the finite Reynolds number with the Sampson flow in lower Reynolds number and ignored the remaining pressure contribution from the larger section of the channels. It has been shown that if the Reynold number

$$\frac{\rho_f V_{\text{max}} r}{\eta_0} > 3.2,$$

where  $\rho_f$  is the fluid density, then inertial effects become more pronounced, so that the contraction  $K_C$  and expansion  $K_E$  term under the finite Reynolds number should be used instead as follows:

$$P_{C+E} = (K_C + K_E)\rho_f V_{\text{max}}^2,$$

where  $K_C + K_E = 1.5$  for a sudden constriction from a large to small area. This was used in the work of Zhang *et al.*<sup>29</sup> In our case, we focus on the low Reynold number regime, i.e., creeping flow without inertial forces.

There are several limitations of the current model. First, only a constant surface tension is considered for the interface so that it cannot be accurately applied for vesicles, capsules, and cells, in which membrane bending stiffness, area conservation, and shear elasticity may play a major role. Although Bruinsma<sup>35</sup> showed that a dynamic surface tension can be used for studying vesicles, and shear elasticity can be incorporated as did in the classical micropipette aspiration analysis, 48 they are not included in the current work and their effects will be explored in the future study. Second, the current model only works for a certain range of physical parameters, such as the flow rate, droplet to pore size ratio, capillary number, etc., the model will give a substantial error beyond these ranges. For example, if the capillary number is quite high, the droplet can break up or form a concave rear shape. If the droplet is small compared to the pore size, then the lubrication theory does not apply. Third, in some cases, we observed a concave shape of the rear part of the droplet in our simulations. In this case, our model assuming a convex rear part will underestimate the transit time because a convex rear part is against the motion while a concave rear part will facilitate the motion. However, this difference should be small because in most cases when the rear part turns concave, it occurs near the end of the process, which is very short. Since the main purpose of this study is to estimate the transit time, the underestimation is small. Finally, a circular and axisymmetric pore is assumed in the current study, but rectangular slit-like cross sections are more frequently used in the existing experiments.<sup>19</sup> We will extend the current model to study the slit-like pore in the future.

#### **ACKNOWLEDGMENTS**

Z.T., L.S., and Z.P. acknowledge the funding support by an REU supplement from the National Science Foundation to the Center for Advanced Design and Manufacturing of Integrated Microfluidics (NSF I-UCRC award number IIP-1841473). Z.P. is also partially supported by NSF/DMS Award No. 1951526 and NSF/CBET 1706436/1948347. F.Y., E.H., and A.V. are supported by the French Government program managed by the French National Research Agency (Grant Nos. ANR-20-CE17-0024 and ANR-16-CONV-0001). E.H., A.V., and Z.P. are also supported by the joint NSF-ANR grant (Grant No. NSF PHY-2210366). E.H. belongs to the French Consortium AQV.

## AUTHOR DECLARATIONS Conflict of Interest

The authors have no conflicts to disclose.

#### **Author Contributions**

Zhengxin Tang: formal analysis (equal); investigation (equal); validation (equal); visualization (equal); writing—original draft (equal); and

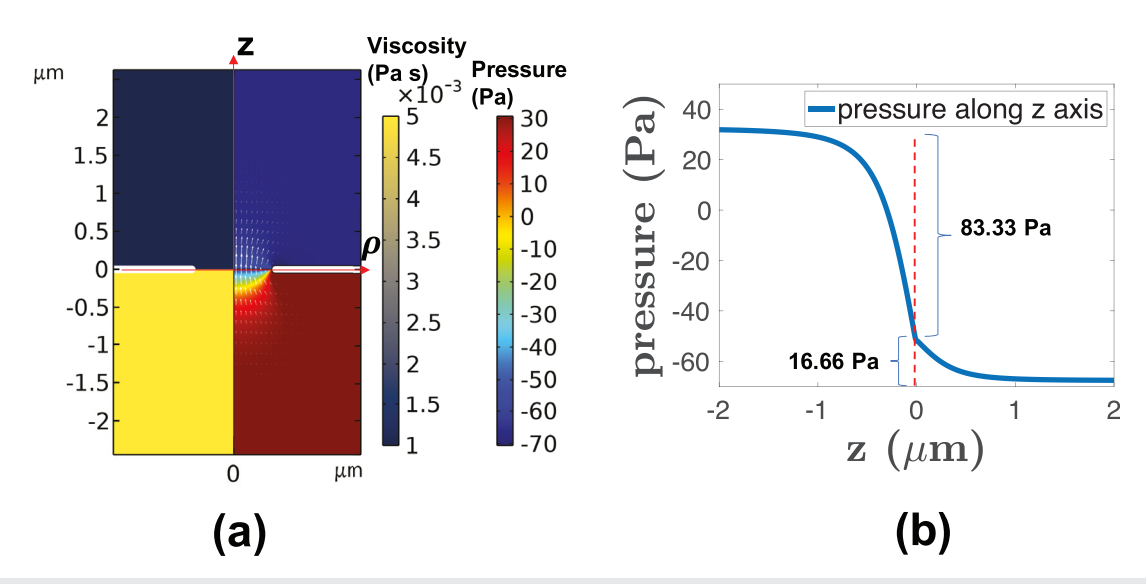


**FIG. 8.** Sampson flow with two fluids. (a) 2D axisymmetric FEM simulations of the Sampson flow with two fluids. The viscosity of the top fluid is 0.001 Pa s, while that of the bottom fluid is 0.005 Pa s. The left half image shows the viscosity, and the right half image shows the pressure contour and velocity vector field (white arrows). (b) The pressure along the z axis. The pore radius is  $r = 0.5 \mu m$ . The flow rate is  $Q = 1.303 \times 10^{-15} \, m^3/s$  and the total pressure drop is 100 Pa. Our theory in Eq. (5) predicts that the top and bottom pressure drops are  $\frac{Q \times 3\eta_0}{2r^3} = 15.64 \, \text{Pa}$ ,  $\frac{Q \times 3\eta_0}{2r^3} = 78.18 \, \text{Pa}$ , while the pressure drops predicted from the simulations are 16.66 and 83.33 Pa, respectively. The small differences between the theory and simulations are caused by the finite thickness of the plate separating the two fluids.

writing—review and editing (equal). François Yaya: investigation (equal) and writing—review and editing (equal). Ethan T. Sun: formal analysis (equal); investigation (equal); visualization (equal); and writing—original draft (equal). Lubna Shah: formal analysis (equal); investigation (equal); visualization (equal); and writing—original draft (equal). Jie Xu: writing—review and editing (equal). Annie Viallat: funding acquisition (equal); project administration (equal); supervision (equal); and writing—review and editing (equal). Emmanuele Helfer: funding acquisition (equal); project administration (equal); supervision (equal); and writing—review and editing (equal). Zhangli Peng: conceptualization (equal); formal analysis (equal); funding acquisition (equal); investigation (equal); project administration (equal); software (equal); supervision (equal); writing—original draft (equal); and writing—review and editing (equal).

#### **DATA AVAILABILITY**

The data that support the findings of this study are available from the corresponding author upon reasonable request.

#### APPENDIX: SAMPSON FLOW WITH TWO FLUIDS

Numerical simulations of Sampson flow with two fluids are shown in Fig. 8.

#### **REFERENCES**

- <sup>1</sup>A. T. S. Cerdeira, J. B. L. M. Campos, J. M. Miranda, and J. D. P. Araújo, "Review on microbubbles and microdroplets flowing through microfluidic geometrical elements," Micromachines 11, 201 (2020).
- <sup>2</sup>I. Chakraborty, J. Ricouvier, P. Yazhgur, P. Tabeling, and A. M. Leshansky, "Droplet generation at Hele-Shaw microfluidic T-junction," Phys. Fluids 31, 022010 (2019).

- <sup>3</sup>S. K. Jena, T. Srivastava, S. S. Bahga, and S. Kondaraju, "Effect of channel width on droplet generation inside T-junction microchannel," Phys. Fluids 35, 022107 (2023).
- <sup>4</sup>M. A. Maleki, M. Soltani, N. Kashaninejad, and N.-T. Nguyen, "Effects of magnetic nanoparticles on mixing in droplet-based microfluidics," Phys. Fluids 31, 032001 (2019).
- <sup>5</sup>A. Sattari, N. Tasnim, P. Hanafizadeh, and M. Hoorfar, "Motion and deformation of migrating compound droplets in shear-thinning fluids in a microcapillary tube," Phys. Fluids 33, 053106 (2021).
- <sup>6</sup>A. Singla and B. Ray, "Effects of surface topography on low Reynolds number droplet/bubble flow through a constricted passage," Phys. Fluids 33, 011301 (2021).
- <sup>7</sup>C. Yang, R. Qiao, K. Mu, Z. Zhu, R. X. Xu, and T. Si, "Manipulation of jet breakup length and droplet size in axisymmetric flow focusing upon actuation," Phys. Fluids 31, 091702 (2019).
- <sup>8</sup>L. Zanini and C. Sada, "Droplet-induced optical effects in an opto-microfluidic cross-configuration system," Phys. Fluids 35, 032007 (2023).
- <sup>9</sup>I. V. Pivkin, Z. Peng, G. E. Karniadakis, P. A. Buffet, M. Dao, and S. Suresh, "Biomechanics of red blood cells in human spleen and consequences for physiology and disease," Proc. Natl. Acad. Sci. U. S. A. 113, 7804 (2016).
- 10 J. Picot, P. A. Ndour, S. D. Lefevre, W. El Nemer, H. Tawfik, J. Galimand, L. Da Costa, J.-A. Ribeil, M. de Montalembert, V. Brousse, B. Le Pioufle, P. Buffet, C. Le Van Kim, and O. Français, "A biomimetic microfluidic chip to study the circulation and mechanical retention of red blood cells in the spleen," Am. J. Hematol. 90, 339 (2015).
- <sup>11</sup>Y.-T. Yeh, R. Serrano, J. François, J.-J. Chiu, Y.-S. J. Li, J. C. del Álamo, S. Chien, and J. C. Lasheras, "Three-dimensional forces exerted by leukocytes and vascular endothelial cells dynamically facilitate diapedesis," Proc. Natl. Acad. Sci. U. S. A. 115, 133 (2018).
- <sup>12</sup>C. R. Pfeifer, J. Irianto, R. R. Bennett, Y. Xia, I. L. Ivanovska, A. J. Liu, R. A. Greenberg, and D. E. Discher, "Nuclear constriction segregates mobile nuclear proteins away from chromatin," Biophys. J. 112, 337a (2017).
  <sup>13</sup>C. R. Pfeifer, J. Irianto, and D. E. Discher, Nuclear Mechanics and Cancer Cell
- <sup>15</sup>C. R. Pfeifer, J. Irianto, and D. E. Discher, Nuclear Mechanics and Cancer Cel Migration (Springer International Publishing, 2019).
- <sup>14</sup> A. J. Lomakin, C. J. Cattin, D. Cuvelier, Z. Alraies, M. Molina, G. P. F. Nader, N. Srivastava, P. J. Sáez, J. M. Garcia-Arcos, I. Y. Zhitnyak, A. Bhargava, M. K. Driscoll, E. S. Welf, R. Fiolka, R. J. Petrie, N. S. De Silva, J. M. González-

- Granado, N. Manel, A. M. Lennon-Duménil, D. J. Müller, and M. Piel, "The nucleus acts as a ruler tailoring cell responses to spatial constraints," Science 370, eaba2894 (2020).
- <sup>15</sup>T. Fujita, "A scanning electron microscope study of the human spleen," Arch. Histol. Jpn. 37, 187 (1974).
- <sup>16</sup>Š. Polák, P. Gálfiová, and I. Varga, "Ultrastructure of human spleen in transmission and scanning electron microscope," <u>Biologia</u> 64, 402 (2009).
- <sup>17</sup>J. K. Chamberlain, L. Weiss, and R. I. Weed, "Bone marrow sinus cell packing: A determinant of cell release," <u>Blood</u> 46, 91 (1975).
- <sup>18</sup>L. G. Rigat-Brugarolas, A. Elizalde-Torrent, M. Bernabeu, M. De Niz, L. Martin-Jaular, C. Fernandez-Becerra, A. Homs-Corbera, J. Samitier, and H. A. del Portillo, "A functional microengineered model of the human splenon-on-a-chip," Lab Chip 14, 1715 (2014).
- <sup>19</sup>P. Gambhire, S. Atwell, C. Iss, F. Bedu, I. Ozerov, C. Badens, E. Helfer, A. Viallat, and A. Charrier, "High aspect ratio sub-micrometer channels using wet etching: Application to the dynamics of red blood cell transiting through biomimetic splenic slits," Small 13, 1700967 (2017).
- <sup>20</sup>A. Moreau, F. Yaya, H. L. Lu, A. Surendranath, A. Charrier, B. Dehapiot, E. Helfer, A. Viallat, and Z. Peng, "Physical mechanisms of red blood cell splenic filtration," Proc. Natl. Acad. Sci. U. S. A.; bioRxiv (preprint).
- <sup>21</sup>J. Duez, J. P. Holleran, P. A. Ndour, C. Pionneau, S. Diakité, C. Roussel, M. Dussiot, P. Amireault, V. M. Avery, and P. A. Buffet, "Mechanical clearance of red blood cells by the human spleen: Potential therapeutic applications of a biomimetic RBC filtration method," Transfus. Clin. Biol. 22, 151 (2015).
- <sup>22</sup>S. Ma, J. M. Sherwood, W. T. S. Huck, and S. Balabani, "On the flow topology inside droplets moving in rectangular microchannels," Lab Chip 14, 3611 (2014).
- 23Y. Wang, M. Do-Quang, and G. Amberg, "Viscoelastic droplet dynamics in a Y-shaped capillary channel," Phys. Fluids 28, 033103 (2016).
- <sup>24</sup>M. I. Gregersen, C. A. Bryant, W. E. Hammerle, S. Usami, and S. Chien, "Flow characteristics of human erythrocytes through polycarbonate sieves," Science 157, 825 (1967).
- 25X. Ren, P. Ghassemi, J. S. Strobl, and M. Agah, "Biophysical phenotyping of cells via impedance spectroscopy in parallel cyclic deformability channels," Biomicrofluidics 13, 044103 (2019).
- <sup>26</sup>Z. S. Khan, N. Kamyabi, F. Hussain, and S. A. Vanapalli, "Passage times and friction due to flow of confined cancer cells, drops, and deformable particles in a microfluidic channel," Convergent Sci. Phys. Oncol. 3, 024001 (2017).
- <sup>27</sup>Z. Zhang, J. Xu, and C. Drapaca, "Particle squeezing in narrow confinements," Microfluid. Nanofluid. 22, 120 (2018).
- <sup>28</sup>Z. Zhang, C. Drapaca, X. Chen, and J. Xu, "Droplet squeezing through a narrow constriction: Minimum impulse and critical velocity," Phys. Fluids 29, 072102 (2017).
- <sup>29</sup>Z. Zhang, C. Drapaca, D. Gritsenko, and J. Xu, "Pressure of a viscous droplet squeezing through a short circular constriction: An analytical model," Phys. Fluids 30, 102004 (2018).

- <sup>30</sup>M. J. Jensen, G. Goranovi, and H. Bruus, "The clogging pressure of bubbles in hydrophilic microchannel contractions," J. Micromech. Microeng. 14, 876 (2004).
- 31A. Marmur, "Penetration of a small drop into a capillary," J. Colloid Interface Sci. 122, 209 (1988).
- <sup>32</sup>G. Gompper and D. M. Kroll, "Driven transport of fluid vesicles through narrow pores," Phys. Rev. E 52, 4198 (1995).
- <sup>53</sup>R. E. Waugh and M. Sassi, "An in vitro model of erythroid egress in bone marrow," <u>Blood</u> 68, 250 (1986).
- <sup>34</sup>F. P. Bretherton, "The motion of long bubbles in tubes," J. Fluid Mech. 10, 166 (1961).
- 35R. Bruinsma, "Rheology and shape transitions of vesicles under capillary flow," Physica A 234, 249 (1996).
- <sup>36</sup>T. W. Secomb, R. Skalak, N. Özkaya, and J. F. Gross, "Flow of axisymmetric red blood cells in narrow capillaries," J. Fluid Mech. 163, 405 (1986).
- <sup>37</sup>D. Barthes-Biesel, Microhydrodynamics and Complex Fluids (CRC Press, 2012).
- 38Z. Zhang, J. Xu, B. Hong, and X. Chen, "The effects of 3D channel geometry on CTC passing pressure—Towards deformability-based cancer cell separation," Lab Chip 14, 2576 (2014).
- 39A. Z. Zinchenko and R. H. Davis, "A boundary-integral study of a drop squeezing through interparticle constrictions," J. Fluid Mech. 564, 227 (2006).
- <sup>40</sup>G. Sampson, "XII. On Stokes's current function," Philos. Trans. R. Soc., A 182, 449 (1891).
- <sup>41</sup>Z. Dagan, S. Weinbaum, and R. Pfeffer, "An infinite-series solution for the creeping motion through an orifice of finite length," J. Fluid Mech. 115, 505 (1982).
- <sup>42</sup>K. Piroird, C. Clanet, and D. Quéré, "Capillary extraction," Langmuir 27, 9396 (2011).
- <sup>43</sup>COMSOL AB, COMSOL Multiphysics\* ver. 6.1 (COMSOL AB, Stockholm, Sweden, 2022).
- <sup>44</sup>H. Lu and Z. Peng, "Boundary integral simulations of a red blood cell squeezing through a submicron slit under prescribed inlet and outlet pressures," Phys. Fluids 31, 031902 (2019).
- 45 Z. Peng, O. S. Pak, Z. Feng, A. P. Liu, and Y.-N. Young, "On the gating of mechanosensitive channels by fluid shear stress," Acta Mech. Sin. 32, 1012 (2016)
- 46 W. L. Olbricht, "Pore-scale prototypes of multiphase flow in porous media," Annu. Rev. Fluid Mech. 28, 187 (1996).
- <sup>47</sup>W. L. Olbricht and D. M. Kung, "The deformation and breakup of liquid drops in low Reynolds number flow through a capillary," Phys. Fluids A 4, 1347 (1992).
- 48R. Waugh and E. A. Evans, "Thermoelasticity of red blood cell membrane," Biophys. J. 26, 115 (1979).